



Cite this: *Phys. Chem. Chem. Phys.*,  
2015, 17, 18670

# Factors influencing the photocatalytic activity of rutile TiO<sub>2</sub> nanorods with different aspect ratios for dye degradation and Cr(vi) photoreduction†

Zewei Yang,<sup>a</sup> Bing Wang,<sup>\*a</sup> Jin Zhang,<sup>b</sup> Hao Cui,<sup>a</sup> Yang Pan,<sup>a</sup> Hao An<sup>a</sup> and Jianping Zhai<sup>a</sup>

Shape-controlled rutile TiO<sub>2</sub> nanorods (NRs) with large {110} and small {111} exposed facets were prepared by hydrothermal treatment of a peroxo titanate acid (PTA) solution. The aspect ratio of the NRs was controlled by the pH of the PTA solution and the addition of polyvinyl alcohol (PVA) or polyvinyl pyrrolidone (PVP). The spatial separation of reduction and oxidation sites, where {110} facets act as reduction sites and {111} facets as oxidation ones, was revealed by tracking the distribution of Pt and PbO<sub>2</sub> deposited on the NR surfaces. The MB degradation activity depended on the aspect ratio of the rutile NRs because of the different separation efficiencies of photo-generated carriers on different facets. Meanwhile, the Cr(vi) reduction activity was governed by the slight shift of the conduction-band potential of the rutile NRs estimated from Mott–Schottky plots, which may be caused by the variation of the content of {110} facets in the rutile NRs. Among the prepared rutile NRs, the sample prepared using a PTA solution at pH 4 containing 10 mg of PVA showed higher activity for photocatalytic Cr(vi) reduction than Degussa P25. These results provide a feasible method to design efficient TiO<sub>2</sub> photocatalysts with tunable photoreactivity for environmental applications.

Received 22nd April 2015,  
Accepted 23rd June 2015

DOI: 10.1039/c5cp02354h

www.rsc.org/pccp

## 1. Introduction

Since Fujishima and Honda's pioneering work in 1972,<sup>1</sup> titanium dioxide (TiO<sub>2</sub>) has been one of the most extensively studied photocatalysts because of its abundance, non-toxicity, and stability.<sup>2</sup> In nature, TiO<sub>2</sub> exists mainly in three crystal phases: anatase, rutile, and brookite. The properties of each crystalline structure are strongly controlled by their physical characteristics, such as size, shape and surface state.<sup>3</sup> Although it is commonly accepted that anatase TiO<sub>2</sub> is the active phase in photocatalysis, rutile TiO<sub>2</sub> still has some advantages over anatase such as higher chemical stability and refractive index.<sup>4</sup> Moreover, rutile TiO<sub>2</sub> has specific exposed facets that work separately as reduction and oxidation sites, which sometimes leads to enhanced photocatalytic activity.<sup>5</sup> Ohno *et al.*<sup>6</sup> found that a redox reaction proceeded preferentially on specific exposed crystal faces of TiO<sub>2</sub>, and this effect was stronger for rutile particles than for anatase ones. Liu and coworkers<sup>7</sup> synthesized a pure rutile photoanode with only

exposed pyramidal {111} facets that exhibited excellent visible-light photoelectrocatalytic activity toward oxidation of water and organic species. In addition, two types of sword-shaped rutile TiO<sub>2</sub> nanostructures with highly reactive {001} or {101} facets have been prepared.<sup>8</sup> The quantitative photocatalytic reactivity of these structures, evaluated by their ability to photoreduce silver, was over an order of magnitude higher than that of a reference low-energy TiO<sub>2</sub>{110} substrate. Hayashi *et al.*<sup>9</sup> successfully synthesized sea urchin-shaped rutile TiO<sub>2</sub> nanocrystals containing numerous needle-like single crystals grown parallel to the {110} face and demonstrated that the {110} facets are able to enhance the photocatalytic degradation of acetaldehyde. It has also been reported that rutile TiO<sub>2</sub> modified at specific sites with Fe<sup>3+</sup> ions shows high photocatalytic activity under visible-light irradiation because of separation of redox sites; *i.e.*, oxidation and reduction proceed at Fe<sup>3+</sup> ions on {111} faces and {110} faces of the bare TiO<sub>2</sub> surface, respectively.<sup>10</sup> These results imply that the type of the exposed crystal face is an important factor affecting the photocatalytic activity of rutile TiO<sub>2</sub>. This is reasonable because the surface energy, chemical surface state, and the number and energy state of defect sites predominantly rely on the atomic arrangement of exposed crystal faces.<sup>11</sup> However, it is difficult to synthesize pure rutile TiO<sub>2</sub> with well-crystallized facets because usually the anatase phase is formed at low temperature by various methods.<sup>12</sup>

<sup>a</sup> State Key Laboratory of Pollution Control and Resource Reuse, and School of the Environment, Nanjing University, Nanjing 210046, P. R. China.

E-mail: bingwang@nju.edu.cn; Fax: +86 25 83592903; Tel: +86 25 83592903

<sup>b</sup> School of Biochemical and Environmental Engineering,

Nanjing Xiaozhuang University, Nanjing 211171, P. R. China

† Electronic supplementary information (ESI) available. See DOI: 10.1039/c5cp02354h

Therefore, it is of fundamental importance to develop mild synthetic techniques that allow the particle shape, nano- and micro-meter scale morphologies, and crystallinity of rutile  $\text{TiO}_2$  to be well defined and controlled.<sup>13</sup>

It is well known that one-dimensional  $\text{TiO}_2$  nanostructures, such as nanotubes, nanorods (NRs) and nanowires, can provide direct electrical pathways for photo-generated electrons and thus increase the rate of electron transport, which in turn improves the photocatalytic performance.<sup>14</sup> In particular,  $\text{TiO}_2$  NRs are believed to have exceptional electron transport properties and have been considered as alternatives to nanoparticles for photocatalysis.<sup>15</sup> Recent research has revealed that the electron diffusion coefficient of single-crystalline rutile  $\text{TiO}_2$  NRs is more than two orders of magnitude higher than that of rutile nanoparticles.<sup>16,17</sup> Although NR-like rutile  $\text{TiO}_2$  has aroused great research interest, most studies to date on photocatalytic oxidation or reduction under ultraviolet (UV) irradiation have focused on anatase  $\text{TiO}_2$  NRs;<sup>18–22</sup> little attention has been paid to rutile  $\text{TiO}_2$  NRs.<sup>23,24</sup>

In this work, rutile  $\text{TiO}_2$  NRs with exposed  $\{110\}$  and  $\{111\}$  facets are prepared by low-temperature hydrothermal synthesis using titanium(IV) ethoxide as the Ti source. The effect of the pH of the peroxy titanate acid (PTA) solution and polymer additives, such as polyvinyl alcohol (PVA) or polyvinyl pyrrolidone (PVP), during hydrothermal treatment on the aspect ratios and crystallinity of the rutile  $\text{TiO}_2$  NRs is examined. We also investigate the photocatalytic performance of the prepared rutile  $\text{TiO}_2$  NRs by assessing their ability to degrade methylene blue (MB) and reduce  $\text{Cr(VI)}$ . The factors affecting the photocatalytic activity of the rutile  $\text{TiO}_2$  NRs in these two catalytic reactions are evaluated. This work allows us to better understand the photocatalytic performance of rutile  $\text{TiO}_2$  NRs with exposed  $\{110\}$  and  $\{111\}$  facets.

## 2. Experimental

### 2.1 Materials

All chemicals were of analytical grade and used without further purification. Materials used in the present study included titanium(IV) ethoxide, ethanol, hydrogen peroxide (30%), ammonia water (25%), glycolic acid (70%), PVA, PVP, MB, potassium dichromate, diphenylcarbazide, 2-propanol, hexachloroplatinic acid ( $\text{H}_2\text{PtCl}_6 \cdot 6\text{H}_2\text{O}$ ), lead nitrate ( $\text{Pb}(\text{NO}_3)_2$ ), and nitric acid (65%). Degussa P25 was produced by Degussa AG, Germany. Sample solutions were prepared using ultrapure water that was obtained by passing deionized water through a Nanopure II deionization system.

### 2.2 Preparation of rutile $\text{TiO}_2$ NRs

Morphology-controlled rutile  $\text{TiO}_2$  NRs with exposed  $\{110\}$  and  $\{111\}$  facets were prepared by a hydrothermal method as follows. Deionized water (3 mL) was added dropwise over 30 min to a vigorously stirred mixture of titanium(IV) ethoxide (10 mL) and ethanol (50 mL) at room temperature. The resulting precipitate was centrifugally separated from the solution and dried under reduced pressure. The obtained amorphous titanium hydroxide

particles were dispersed in hydrogen peroxide (40 mL). Ammonia water (1 mL) as a regulator and glycolic acid (1.6 mL) as a shape-control reagent were added. The solution was stirred at room temperature for 10 h to remove excess hydrogen peroxide and ammonia to form a PTA solution. The pH of the PTA solution was adjusted to the desired value using ammonia. The PTA solution (40 mL) was transferred into a 50 mL Teflon-lined stainless steel autoclave, and then treated hydrothermally at 180 °C for 48 h. After cooling the autoclave to room temperature, the product was centrifuged to remove the supernatant, washed with distilled water several times and then dried under vacuum at 60 °C for 12 h. The final products are denoted as NR-*a*, where *a* is the pH of the corresponding PTA solution.

To prepare rutile  $\text{TiO}_2$  NRs using PVA or PVP to control the aspect ratio, ammonia solution (1 mL) and glycolic acid (1.6 mL) were added to an aqueous solution containing an appropriate amount of PVA or PVP (10 mg and 20 mg). The resulting solution was stirred at room temperature for 10 h to remove excess hydrogen peroxide, and give a PTA solution. The pH of the PTA solution was adjusted to 4 by addition of ammonia. The subsequent steps were the same as those described above in the preparation of rutile  $\text{TiO}_2$  NRs without polymer. The final products are denoted as NR-4, PVA or PVP-*b*, where *b* represents the number of milligrams of PVA or PVP.

### 2.3 Photodeposition of Pt and $\text{PbO}_2$ on rutile $\text{TiO}_2$ NRs

To deposit Pt on the rutile  $\text{TiO}_2$  NRs, an aqueous NR-4 suspension ( $2 \text{ g L}^{-1}$ ) containing 2-propanol (0.52 M) and  $\text{H}_2\text{PtCl}_6 \cdot 6\text{H}_2\text{O}$  (1 mM) was irradiated using a 300 W xenon lamp for 24 h.  $\text{N}_2$  gas was purged through the suspension prior to irradiation to remove oxygen. After irradiation, the suspension was centrifuged, washed with ultrapure water and then collected as a powder after drying at 80 °C under reduced pressure for 5 h. The NR-4/Pt powder was used as the catalyst on which  $\text{Pb}^{2+}$  ions were oxidized to form  $\text{PbO}_2$ . For this photocatalytic reaction, NR-4/Pt ( $2 \text{ g L}^{-1}$ ) was dispersed in an aqueous solution of  $\text{Pb}(\text{NO}_3)_2$  (0.1 M) and the pH of the suspension was adjusted to 1.0 by addition of a nitric acid solution. The suspension was irradiated using a 500 W xenon lamp for 24 h. The product was centrifuged, washed with ultrapure water several times and then dried under vacuum at 80 °C for 5 h.

### 2.4 Characterization of prepared samples

X-ray diffraction (XRD) patterns were recorded on an X-ray diffractometer (X'TRA, ARL, Switzerland) using  $\text{Cu-K}\alpha$  radiation. High-resolution transmission electron microscopy (HRTEM) and energy-dispersive X-ray (EDX) analysis of the prepared  $\text{TiO}_2$  particles were performed using a transmission electron microscope (JEM-200CX, JEOL, Japan). Average lengths ( $L_{\text{ave}}$ ) and average widths ( $W_{\text{ave}}$ ) were estimated by TEM observation of more than 90 particles, and the aspect ratio ( $r_{\text{asp}}$ ) of the particles was determined from  $r_{\text{asp}} = L_{\text{ave}}/W_{\text{ave}}$ . The Brunauer–Emmett–Teller (BET) surface areas ( $S_{\text{BET}}$ ) of the particles were evaluated using a nitrogen adsorption apparatus (ASAP2010, Micromeritics, USA) at 77 K. UV-vis absorption spectra of the contaminants were measured using a spectrophotometer

(UV-2550PC, Shimadzu, Kyoto, Japan). Photoluminescence spectra were recorded using a fluorescence spectrometer (Fluorolog-3-Tau, Jobin Yvon, France) using a Xe lamp as the excitation source. UV-vis diffuse reflectance spectra were recorded on a UV-vis spectrometer (UV-3600 PC, Shimadzu, Japan) with barium sulfate as a reference.

## 2.5 Photocatalytic experiments

The photocatalytic oxidation activity of the rutile NRs was measured by their ability to degrade MB (20 mg L<sup>-1</sup>), while their reduction activity was evaluated by their ability to reduce Cr(vi) (10 mg L<sup>-1</sup>). The target contaminants and photocatalysts were placed in a quartz vessel with a diameter of 5.8 cm and a length of 68 cm. A 500 W high-pressure mercury lamp with a principal wavelength of 365 nm served as the UV light source. The photon flux ( $\varphi$ ) of the UV radiation reaching the exposed inner part of the reactor was  $5 \times 10^{-6}$  mol of photon s<sup>-1</sup>. The lamp was surrounded by a quartz jacket in which cooling water was circulated to maintain a constant temperature of 24 °C. Each suspension containing photocatalyst (1 g L<sup>-1</sup>) was stirred in the dark for 1 h to reach the adsorption-desorption equilibrium. After a given irradiation time, an aliquot (3 mL) of the dispersion was removed and centrifuged to separate the photocatalyst. MB was diluted 2-fold, and then analyzed by UV-vis absorption measurement of its characteristic peak at 664 nm to determine the remaining content. The content of Cr(vi) remaining was analyzed using diphenylcarbazide as a developer by UV-vis spectroscopy at 540 nm. The photocatalytic reaction on the surface of the NRs followed pseudo-first order kinetics that can be expressed as:

$$-\ln(C/C_0) = kt \quad (1)$$

where  $k$  is the pseudo-first order rate constant,  $t$  is the time, and  $C$  and  $C_0$  are the reactant concentrations at time  $t = t$  and 0, respectively.

## 2.6 Detection of hydroxyl radicals

The detection of hydroxyl (OH) radicals was done using coumarin as a fluorescent probe.<sup>25</sup> Coumarin reacts with OH radicals to form the fluorescent compound umbelliferone (Scheme S1, ESI<sup>†</sup>), the concentration of which can then be detected by fluorescence measurements. The same equipment and UV source mentioned above were used for this measurement. Rutile NRs (40 mg) were suspended in an aqueous solution of coumarin (1 mM, 40 mL) to give a suspension containing 1 g L<sup>-1</sup> of photocatalyst. The suspension was stirred in the dark for 1 h to reach the adsorption-desorption equilibrium. After a given irradiation time, an aliquot (3 mL) of the dispersion was centrifuged to separate the photocatalyst. The fluorescent product of coumarin, umbelliferone, was diluted 2-fold, and then analyzed by fluorescence measurements using an excitation wavelength of 332 nm. The increase of the fluorescence intensity of umbelliferone at 454 nm was proportional to its concentration.

## 2.7 Flat-band potential measurement

The flat-band potential  $E_{fb}$  of the NRs was measured by impedance spectroscopy using Mott-Schottky plots. The measurements were performed in a conventional thermostated (25 °C) three-electrode cell with a 1 cm<sup>2</sup> platinum sheet as the counter electrode and a saturated calomel electrode (SCE) as the reference electrode. The working electrode was prepared as follows: rutile NRs (10 mg) were dispersed homogeneously in water (1 mL) by sonication. The rutile NR suspension (6  $\mu$ L) was added dropwise onto a glassy carbon electrode, which was subsequently dried under infrared light. Impedance experiments were performed in an aqueous solution of KCl (0.1 M) at pH 7.0. The potential was systematically cycled between -0.8 and +0.4 V vs. SCE at frequencies of 10, 100 and 1000 Hz.

The  $E_{fb}$  values of the rutile NRs at the semiconductor/electrolyte junction were obtained from Mott-Schottky plots (measured in the dark) using the following equation:

$$\frac{1}{C^2} = \frac{2}{\epsilon_{TiO_2} \times \epsilon_0 \times e_0 \times N_D} \left( E - E_{fb} - \frac{\alpha T}{e_0} \right) \quad (2)$$

where  $C$  represents the space charge capacitance,  $\epsilon_{TiO_2}$  is the dielectric constant of the TiO<sub>2</sub> layer,  $\epsilon_0$  is the permittivity of free space,  $e_0$  is the elementary charge,  $N_D$  is the donor density,  $E$  is the applied potential,  $\alpha$  is the Boltzmann constant, and  $T$  is the temperature of operation. A plot of  $(1/C^2)$  against  $E$  (vs. normal hydrogen electrode, NHE) should yield a straight line.  $E_{fb}$  of each sample was estimated by extrapolating the line of the relevant Mott-Schottky plot to the potential at  $1/C^2 = 0$ .

# 3. Results and discussion

## 3.1 Characterization

XRD patterns of the prepared TiO<sub>2</sub> NRs are presented in Fig. 1. The structures of the samples were all consistent with single-phase rutile TiO<sub>2</sub> (JCPDS No. 21-1276). Fig. S1 (ESI<sup>†</sup>) shows TEM images and histograms of the widths and lengths of samples NR-4-8 with rod-like morphology. The average width and length of the rutile NRs were  $W_{ave} = 16-41$  nm and  $L_{ave} = 60-127$  nm.  $S_{BET}$  and  $r_{asp}$  of samples NR-4-8 are depicted in Fig. 2(a) and (b), respectively. Assignment of the exposed facets was confirmed by XRD (Fig. 1) and HRTEM (Fig. 2(c)). TiO<sub>2</sub> NRs with large {110} and small {111} exposed facets and crystal growth in the [001] direction were obtained, as shown in Fig. 2(d).

## 3.2 Photodeposition of Pt and PbO<sub>2</sub> to identify oxidation and reduction sites

To determine the oxidation and reduction sites on the exposed facets of the rutile TiO<sub>2</sub> NRs, photodeposition of Pt and PbO<sub>2</sub> was carried out.<sup>6</sup> Pt and PbO<sub>2</sub> particles were deposited on the surface of the rutile TiO<sub>2</sub> NRs by weak UV irradiation in the presence of H<sub>2</sub>PtCl<sub>6</sub> and Pb(NO<sub>3</sub>)<sub>2</sub>, which were formed by photoreduction ( $Pt^{4+} + 4e^- \rightarrow Pt$ ) and photooxidation ( $Pb^{2+} + 2H_2O + 2h^+ \rightarrow PbO_2 + 4H^+$ ) reactions, respectively. Fig. 3 shows TEM images of Pt- and PbO<sub>2</sub>-deposited NR-4 without polymer

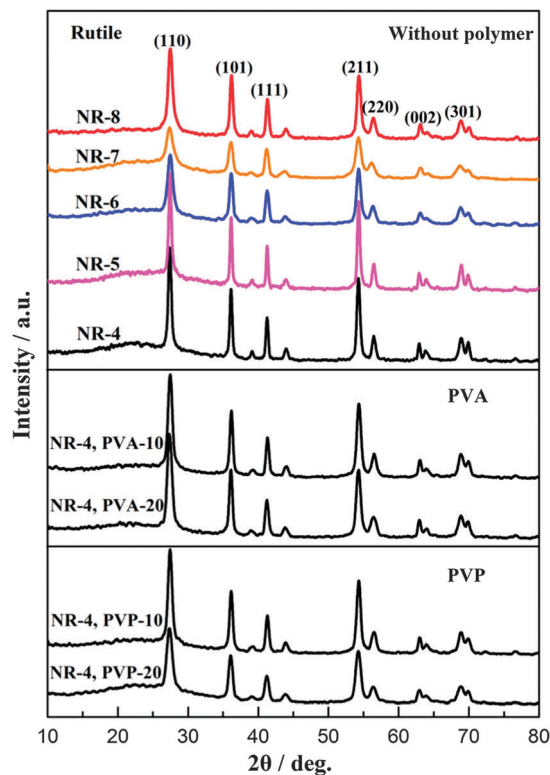


Fig. 1 XRD patterns of samples NR-4–8 without polymer and NR-4 samples with different amounts of PVA or PVP.

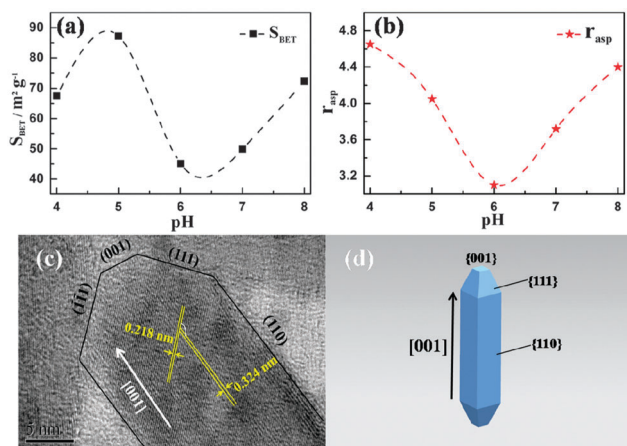


Fig. 2 (a)  $S_{\text{BET}}$  and (b)  $r_{\text{asp}}$  of samples NR-4–8 prepared without polymer. (c) HRTEM image and (d) structure diagram of NR-4.

and corresponding energy-dispersive X-ray (EDX) analysis. Small particles with a size of *ca.* 3 nm were mainly observed on the {110} facets of NR-4. These small particles were assigned to Pt particles according to the results of EDX analysis, and indicate that the side {110} facets can be considered as reduction sites. Likewise, the TEM image depicted in Fig. 3(b) shows that the  $\text{PbO}_2$  particles were deposited as aggregates on the {111} facets, which can therefore be considered as the oxidation sites of the rutile NRs.

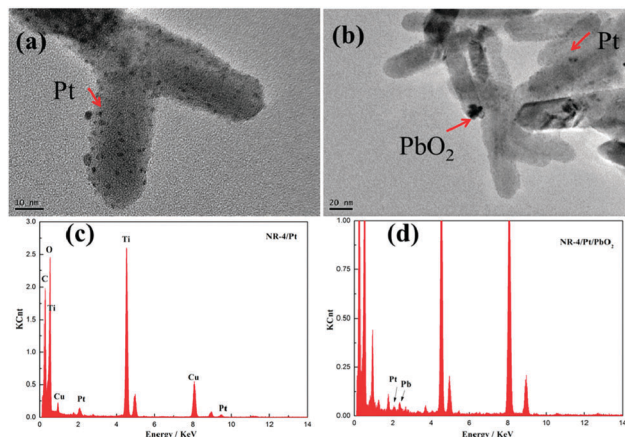


Fig. 3 TEM images of the NR-4 sample on which (a) Pt particles, and (b) Pt and  $\text{PbO}_2$  particles were deposited. EDX analysis of (c) NR-4/Pt and (d) NR-4/Pt/ $\text{PbO}_2$ .

### 3.3 Photocatalytic activity of rutile NRs in MB degradation and $\text{Cr}(\text{vi})$ reduction

The photocatalytic activity of the rutile NRs was evaluated by their photocatalytic degradation of MB and photocatalytic reduction of  $\text{Cr}(\text{vi})$ . Fig. S2 (ESI†) shows the photocatalytic evolution of these systems under UV irradiation. The first-order kinetic rate constants ( $k$ ) during the initial 30 min of photocatalytic reaction are displayed in Fig. 4. Accurate  $k$  values are crucial to investigate the factors that affect the activity of a photocatalyst. Therefore, photocatalytic experiments in this work were conducted at least three times to ensure the sufficient precision of data. The information related to  $S_{\text{BET}}$ ,  $r_{\text{asp}}$ ,  $E_{\text{fb}}$ ,  $k_{\text{MB}}$ , and  $k_{\text{Cr}(\text{vi})}$  is given in Table 1. The general orders of photocatalytic activity were  $\text{NR-4} > \text{NR-8} > \text{NR-5} > \text{NR-7} > \text{NR-6}$  for photocatalytic degradation of MB and  $\text{NR-7} > \text{NR-8} > \text{NR-6} > \text{NR-4} > \text{NR-5}$  for photocatalytic reduction of  $\text{Cr}(\text{vi})$ . These orders reveal that  $S_{\text{BET}}$  (Fig. 2(a)) was not the main factor affecting the rates of photocatalytic redox reactions for the rutile NRs. In the following discussion, the parameters influencing the photocatalytic activity of the rutile NRs are evaluated.

We have also studied the stability of NRs by monitoring the photocatalytic activity for degradation of MB (using NR-4) and reduction of  $\text{Cr}(\text{vi})$  (using NR-7) during three cycles (Fig. S3, ESI†). After each run, samples were recovered by centrifugation, dried at  $80^\circ\text{C}$  for 5 h, and reused for photocatalysis. No significant change could be seen in the photocatalytic activity of the recycled photocatalyst after three cycles, indicating that NRs were stable and effective for the removal of MB or  $\text{Cr}(\text{vi})$  from water.

Fig. 4(a) shows the variation of  $k$  for MB degradation ( $k_{\text{MB}}$ ) for samples NR-4–8. The change of  $k_{\text{MB}}$  was consistent with that of  $r_{\text{asp}}$  (see Fig. 2(b)).  $r_{\text{asp}}$  was defined as the ratio of the maximum length along the [001] direction to that along the [110] direction determined from TEM images. There is a clear linear correlation between  $k_{\text{MB}}$  and  $r_{\text{asp}}$ , and their Pearson correlation coefficient is about 0.96 (Fig. S4(a), ESI†).  $k_{\text{MB}}$  increased with  $r_{\text{asp}}$ , which suggests that  $r_{\text{asp}}$  plays an important role in the photocatalytic activity of rutile NRs for MB degradation. Matsumura<sup>6</sup> and



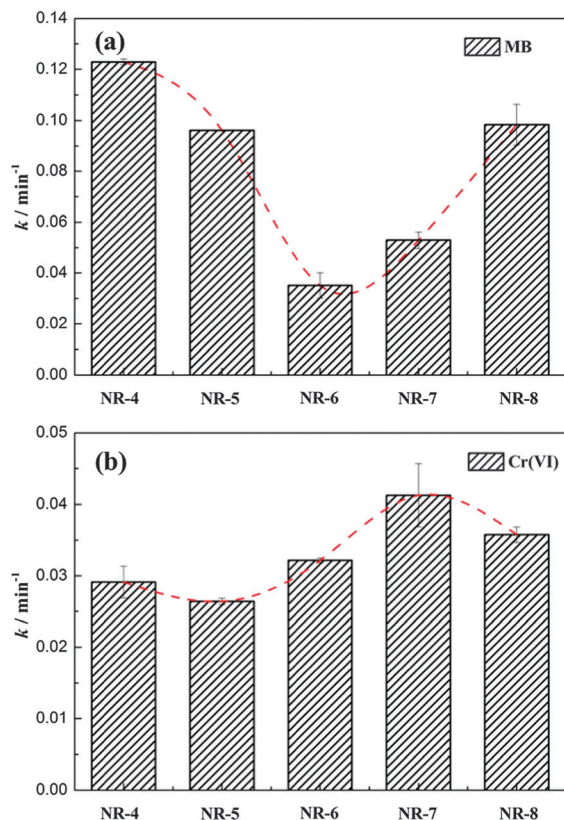


Fig. 4 Rate constants ( $k$ ) for the initial 30 min of photocatalytic (a) degradation of MB and (b) reduction of Cr(VI).

Ohno<sup>11</sup> and coworkers believe that the surface structure of photocatalysts is a factor that determines their photocatalytic activity. Different crystal facets of  $\text{TiO}_2$  possess conduction bands (CBs) and valence bands (VBs) with different energy levels because of the characteristic atomic arrangements of these facets. The difference in the energy levels of facets drives the electrons and holes to different crystal facets that then act as reduction and oxidation sites separately. The separation of photo-generated carriers ( $e^-/h^+$  pairs) is probably the reason for the high efficiency of some photocatalytic reactions. In this work, the  $\{110\}$  and  $\{111\}$  facets of the NRs observed by HRTEM (Fig. 2(c)) showed separation of redox sites because of the preferential deposition of Pt and  $\text{PbO}_2$ , respectively, on them. The different  $r_{\text{asp}}$  of the rutile NRs suggests that there is a distinct separation ratio of redox sites, resulting in different separation efficiencies of the photo-generated carriers. This separation efficiency determines the quantity of OH radicals generated

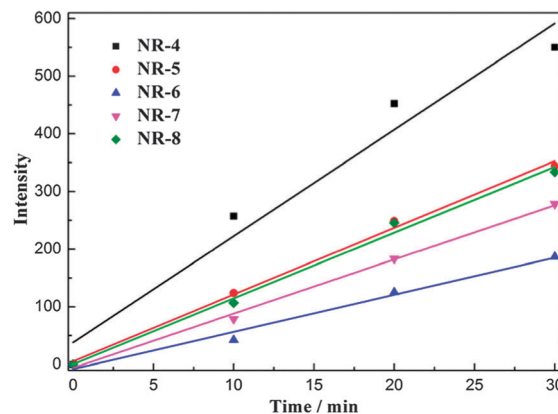


Fig. 5 Fluorescence intensity of umbelliferone produced during the initial 30 min of photocatalytic degradation of MB by NR-4–8.

in reaction systems, which was confirmed as the main active species in photocatalytic MB degradation in our previous study.<sup>26</sup> Thus, the relationship between  $r_{\text{asp}}$  and  $k_{\text{MB}}$  could be explained by considering the relationship between the quantity of OH radicals and  $k_{\text{MB}}$ .

To investigate the amount of OH radicals generated during photocatalytic MB degradation, coumarin was used as a probe molecule for  $\bullet\text{OH}$  detection (see Scheme S1, ESI<sup>†</sup>). Fig. 5 depicts plots of the fluorescence intensity of umbelliferone in the presence of samples NR-4–8. The intensity of fluorescence increased over time, implying that the amount of  $\bullet\text{OH}$  in the dispersion increased. The relative slope for each sample indicated that the general order of the concentration of  $\bullet\text{OH}$  produced in the initial 30 min was  $\text{NR-4} > \text{NR-8} > \text{NR-5} > \text{NR-7} > \text{NR-6}$ , which reflects that of  $k_{\text{MB}}$ . This result confirms that the photocatalytic degradation of MB was governed by OH radicals, which can be used to interpret the positive correlation between  $r_{\text{asp}}$  and  $k_{\text{MB}}$ .

To explain the variation of  $k$  for Cr(VI) reduction ( $k_{\text{Cr(VI)}}$ ) shown in Fig. 4(b), Mott-Schottky plots and UV-vis diffuse reflectance spectra were used to investigate  $E_{\text{fb}}$  and the band-gap ( $E_{\text{g}}$ ) of the rutile NRs; these data are shown in Fig. S5 (ESI<sup>†</sup>).  $E_{\text{fb}}$  of each sample was estimated by extrapolating the line of the Mott-Schottky plots to the potential at  $1/C^2 = 0$ .  $E_{\text{fb}}$  of NR-4, NR-5, NR-6, NR-7 and NR-8 were  $-0.35$ ,  $-0.36$ ,  $-0.40$ ,  $-0.48$  and  $-0.44$  V vs. NHE, respectively.  $E_{\text{fb}}$  equals the Fermi level ( $E_{\text{F}}$ ) for n-type semiconductors such as  $\text{TiO}_2$ , while the CB potential ( $E_{\text{CB}}$ ) is very close to  $E_{\text{F}}$  and depends on the electron effective mass and carrier concentration.<sup>27,28</sup> Thus, according to  $E_{\text{fb}}$  and  $E_{\text{g}}$ , the relative positions of the CB and VB of NR-4–8 samples were suggested as illustrated in Fig. 6. The change of CB potential

Table 1 The information related to the  $S_{\text{BET}}$ ,  $r_{\text{asp}}$ ,  $E_{\text{fb}}$ ,  $k_{\text{MB}}$  and  $k_{\text{Cr(VI)}}$  of sample NRs

Samples	NR-4	NR-5	NR-6	NR-7	NR-8	NR-4, PVP-10	NR-4, PVP-20	NR-4, PVA-10	NR-4, PVA-20
$S_{\text{BET}}$	67.47	87.24	45.08	49.90	72.29	85.81	117.73	96.40	111.10
$r_{\text{asp}}$	4.65	4.05	3.10	3.72	4.40	3.70	3.55	3.96	3.62
$E_{\text{fb}}$	$-0.35$	$-0.36$	$-0.40$	$-0.48$	$-0.44$	$-0.50$	$-0.42$	$-0.57$	$-0.46$
$k_{\text{MB}}$	0.123	0.096	0.035	0.053	0.098	0.090	0.079	0.083	0.076
$k_{\text{Cr(VI)}}$	0.029	0.026	0.032	0.041	0.036	0.060	0.034	0.086	0.050

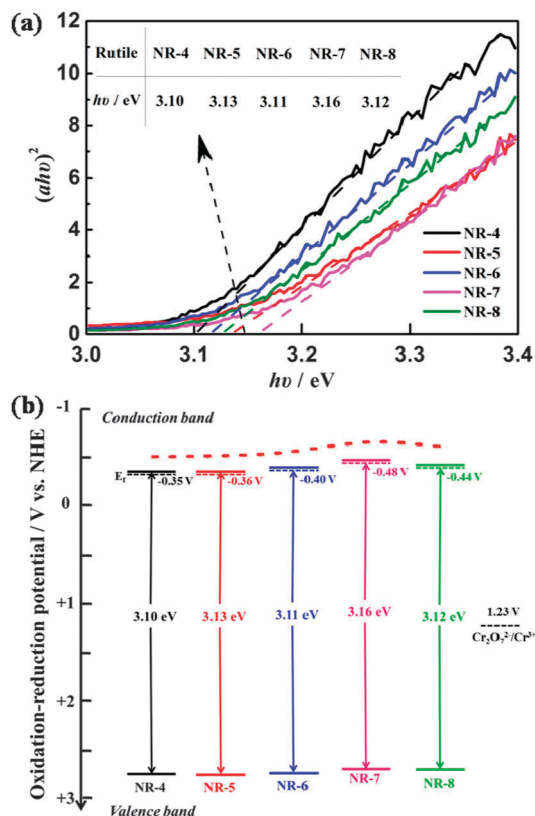


Fig. 6 (a) Plots of  $(\alpha h\nu)^2$  versus energy ( $h\nu$ ) and (b) relative CB and VB positions for NR-4–8.

corresponded well with that of  $k_{\text{Cr(VI)}}$ . The linear relationship between  $k_{\text{Cr(VI)}}$  and  $E_{\text{fb}}$  is plotted in Fig. S4(b) (ESI†) and their Pearson correlation coefficient was about  $-0.97$ . Therefore, we conclude that the CB potential plays an important role in the photocatalytic activity of the rutile NRs in Cr(vi) reduction. A cathodic shift of the CB potential can effectively increase the energy of photo-generated electrons in the rutile NRs, thus enhancing the photocatalytic activity for Cr(vi) reduction. The shifts of CB potential may be caused by the slightly different percentages of  $\{110\}$  facets in the rutile NRs, which were identified as reduction sites during photocatalysis (see Fig. 3(a)).

### 3.4 Effect of PVA or PVP used to control the aspect ratio of rutile NRs on their photocatalytic activity for MB degradation and Cr(vi) reduction

To further confirm the important roles of  $r_{\text{asp}}$  and CB potential of the NRs in photocatalytic MB degradation and Cr(vi) reduction, respectively, we synthesized a series of NRs using different amounts of PVA or PVP. The XRD patterns in Fig. 1 reveal that the NR-4 samples with different amounts of PVA or PVP were still single-phase rutile  $\text{TiO}_2$ . TEM images and corresponding histograms (Fig. S6, ESI†) suggested that the addition of PVA or PVP allowed  $r_{\text{asp}}$  of the rutile NRs to be controlled. The average width and length of NR-4 with PVA or PVP were  $W_{\text{ave}} = 11\text{--}15$  nm and  $L_{\text{ave}} = 40\text{--}55$  nm, respectively. The NR-4 sample without polymer (Fig. S6(a), ESI†) possessed the largest  $r_{\text{asp}}$  of 4.65, and

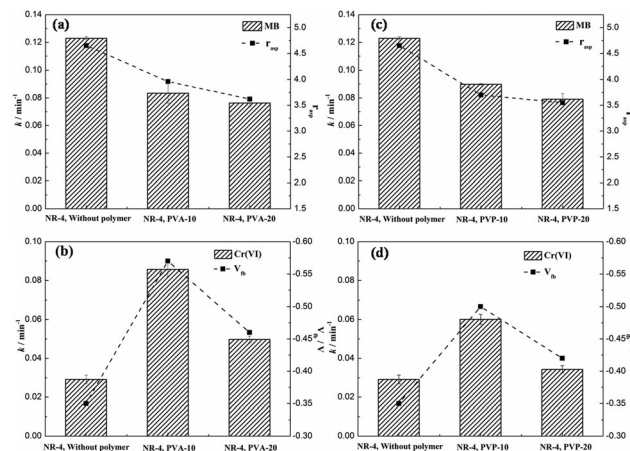


Fig. 7 (a), (c)  $k$  and  $r_{\text{asp}}$ , and (b), (d)  $k$  and  $E_{\text{fb}}$  of NR-4 samples synthesized without polymer and with different amounts of PVA or PVP for photocatalytic MB degradation and Cr(vi) reduction.

$r_{\text{asp}}$  decreased as the amount of PVA or PVP added increased (Fig. S6(b–e), ESI†). The ability of PVP to control the aspect ratio of the rutile NRs was greater than that of PVA.

The photocatalytic evolution of NR-4 samples with PVA or PVP under UV irradiation was investigated (Fig. S7, ESI†), and Mott–Schottky plots were drawn (Fig. S8, ESI†).  $k$  for MB degradation and Cr(vi) reduction along with related  $r_{\text{asp}}$  and  $E_{\text{fb}}$  of NR-4 samples without and with PVA or PVP are displayed in Fig. 7.  $k_{\text{MB}}$  decreased with  $r_{\text{asp}}$  (Fig. 7(a) and (c)). The Pearson correlation coefficients between  $k_{\text{MB}}$  and  $r_{\text{asp}}$  exceeded 0.98 and 0.99 for the samples with PVA and PVP, respectively (Fig. S9(a) and (c), ESI†). These results further indicate that  $r_{\text{asp}}$  strongly affects the photocatalytic activity of the rutile NRs in MB degradation. Similarly, the variation of  $k_{\text{Cr(VI)}}$  was consistent with that of  $E_{\text{fb}}$  for the samples synthesized using PVA (Fig. 7(b)) and PVP (Fig. 7(d)), and their Pearson correlation coefficients were about  $-0.98$  (Fig. S9(b), ESI†) and  $-0.94$  (Fig. S9(d), ESI†), respectively. Therefore, the order of activity for Cr(vi) photocatalytic reduction is governed by the slight shift of CB potential of the rutile NRs. Notably, the photocatalytic reduction activity of NR-4 samples with PVA or PVP were higher than that of the NR-4 sample without polymer. The NR-4, PVA-10 sample exhibited the highest  $k_{\text{Cr(VI)}}$ , which was 1.5 times greater than that of Degussa P25 (Fig. S10, ESI†), because of its most negative CB potential ( $E_{\text{fb}} = -0.57$  V vs. NHE).

## 4. Conclusion

Rutile  $\text{TiO}_2$  NRs with exposed  $\{110\}$  and  $\{111\}$  facets were prepared by low-temperature hydrothermal treatment using PVA or PVP to control their aspect ratio. The  $\{110\}$  and  $\{111\}$  facets of the NRs were found to act as reduction and oxidation sites, respectively.  $r_{\text{asp}}$  of the prepared rutile NRs was controlled by the pH of the PTA solution and the concentration of the aspect-ratio-control reagent during hydrothermal treatment. The rutile NRs also showed different CB potentials, which were

estimated from Mott-Schottky plots. Photocatalytic MB degradation and Cr(vi) reduction using the prepared samples NR-4–8 were carried out. The rutile NRs with higher aspect ratios showed higher photocatalytic activity for MB degradation than those with lower aspect ratios. Therefore, optimization of  $r_{\text{asp}}$  is an important strategy to improve the photocatalytic oxidation activity of rutile NRs. The photocatalytic activity for Cr(vi) reduction was governed by the CB potential of the rutile NRs. The NR-4, PVA-10 sample exhibited the highest  $k$  for photocatalytic Cr(vi) reduction because of its most negative CB potential ( $E_{\text{fb}} = -0.57$  V vs. NHE).

## Acknowledgements

The authors gratefully acknowledge financial support from the Foundation of the State Key Laboratory of Pollution Control and Resource Reuse of China, the National Natural Science Foundation of China (No. 51308282), and a foundation research project of Jiangsu province (Natural Science Foundation of China) – Youth Fund Project (No. BK20130574).

## References

- 1 A. Fujishima and K. Honda, *Nature*, 1972, **238**, 37–38.
- 2 L. Ye, J. Mao, T. Peng, L. Zan and Y. Zhang, *Phys. Chem. Chem. Phys.*, 2014, **16**, 15675–15680.
- 3 F. Zuo, K. Bozhilov, R. J. Dillon, L. Wang, P. Smith, X. Zhao, C. Bardeen and P. Feng, *Angew. Chem., Int. Ed.*, 2012, **51**, 6223–6226.
- 4 L. Sun, Y. Qin, Q. Cao, B. Hu, Z. Huang, L. Ye and X. Tang, *Chem. Commun.*, 2011, **47**, 12628–12630.
- 5 T. Ohno, T. Higo, N. Murakami, H. Saito, Q. Zhang, Y. Yang and T. Tsubota, *Appl. Catal., B*, 2014, **152–153**, 309–316.
- 6 T. Ohno, K. Sarukawa and M. Matsumura, *New J. Chem.*, 2002, **26**, 1167–1170.
- 7 X. Liu, H. Zhang, X. Yao, T. An, P. Liu, Y. Wang, F. Peng, A. R. Carroll and H. Zhao, *Nano Res.*, 2012, **5**, 762–769.
- 8 B. D. Sosnowchik, H. C. Chiamori, Y. Ding, J.-Y. Ha, Z. L. Wang and L. Lin, *Nanotechnology*, 2010, **21**, 485601.
- 9 K. Hayashi, M. Nakamura, Y. Makita, R. Fujiwara, T. Kori and K. Ishimura, *Mater. Lett.*, 2011, **65**, 3037–3040.
- 10 N. Murakami, A. Ono, M. Nakamura, T. Tsubota and T. Ohno, *Appl. Catal., B*, 2010, **97**, 115–119.
- 11 N. Murakami, S. Katayama, M. Nakamura, T. Tsubota and T. Ohno, *J. Phys. Chem. C*, 2011, **115**, 419–424.
- 12 X. Huang and C. Pan, *J. Cryst. Growth*, 2007, **306**, 117–122.
- 13 E. Bae, N. Murakami and T. Ohno, *J. Mol. Catal. A: Chem.*, 2009, **300**, 72–79.
- 14 H. Zhang, X. Liu, Y. Li, Q. Sun, Y. Wang, B. J. Wood, P. Liu, D. Yang and H. Chao, *J. Mater. Chem.*, 2012, **22**, 2465–2472.
- 15 S. H. Kang, S. H. Choi, M. S. Kang, J. Y. Kim, H. S. Kim, T. Hyeon and Y. E. Sung, *Adv. Mater.*, 2008, **20**, 54–58.
- 16 X. Feng, K. Zhu, A. J. Frank, C. A. Grimes and T. E. Mallouk, *Angew. Chem., Int. Ed.*, 2012, **51**, 2727–2730.
- 17 Y. Rui, Y. Li, Q. Zhang and H. Wang, *Nanoscale*, 2013, **5**, 12574–12581.
- 18 P. D. Cozzoli, A. Kornowski and H. Weller, *J. Am. Chem. Soc.*, 2003, **125**, 14539–14548.
- 19 J. N. Nian and H. Teng, *J. Phys. Chem. B*, 2006, **110**, 4193–4198.
- 20 Y. Yu and D. Xu, *Appl. Catal., B*, 2007, **73**, 166–171.
- 21 C. Wang, X. Zhang, Y. Zhang, Y. Jia, B. Yuan, J. Yang, P. Sun and Y. Liu, *Nanoscale*, 2012, **4**, 5023–5030.
- 22 W. Zhang, Y. Xie, D. Xiong, X. Zeng, Z. Li, M. Wang, Y. B. Cheng, W. Chen, K. Yan and S. Yang, *ACS Appl. Mater. Interfaces*, 2014, **6**, 9698–9704.
- 23 Y. Wang, L. Zhang, K. Deng, X. Chen and Z. Zou, *J. Phys. Chem. C*, 2007, **111**, 2709–2714.
- 24 E. Bae and T. Ohno, *Appl. Catal., B*, 2009, **91**, 634–639.
- 25 J. Zhang and Y. Nosaka, *J. Phys. Chem. C*, 2014, **118**, 10824–10832.
- 26 B. Wang, C. Li, H. Cui, J. Zhang, J. Zhai and Q. Li, *J. Mater. Sci.*, 2014, **49**, 1336–1344.
- 27 E. Gao, W. Wang, M. Shang and J. Xu, *Phys. Chem. Chem. Phys.*, 2011, **13**, 2887–2893.
- 28 A. Ishikawa, T. Takata, J. N. Kondo, M. Hara, H. Kobayashi and K. Domen, *J. Am. Chem. Soc.*, 2002, **124**, 13547–13553.